

AA241X: DESIGN, CONSTRUCTION, AND TESTING OF AUTONOMOUS AIRCRAFT



FINAL REPORT June 9, 2014

Authors:

Kartikey Asthana
kasthana@stanford.edu

Peter Blake
psblake@stanford.edu

Brandon Jennings
bjennin@stanford.edu

Erik Moon
emoon1@stanford.edu

Sravya Nimmagadda
sravya@stanford.edu

Akshay Subramaniam
akshays@stanford.edu

Ian Villa
ianvilla@stanford.edu

Jerry Watkins
watkins2@stanford.edu

Degree & Department:

Ph.D. Candidate
Aeronautics & Astronautics

M.S. Candidate
Graduate School of Business

M.S. Candidate
Mechanical Engineering

M.S. Candidate
Graduate School of Business

Ph.D. Candidate
Aeronautics & Astronautics

Ph.D. Candidate
Aeronautics & Astronautics

B.S. & M.S. Candidate
Aeronautics & Astronautics

Ph.D. Candidate
Aeronautics & Astronautics

Contents

1	Introduction	3
2	The Team	3
2.1	Team Structure	3
2.2	Team Communication & Logistics	3
3	Mission	4
3.1	Approach via identification of score components	4
3.2	Phase-1: An initial passive path to sight all targets with probability 1	4
3.3	Phase-2: An active path to refine the estimates of sighted targets	6
3.4	Target position estimation scheme	9
3.5	Statistical measure of score and mission time	12
4	Airframe Design	15
4.1	Propulsion System Analysis	15
4.1.1	Propeller Analysis	15
4.1.2	Motor Analysis	15
4.1.3	Propeller and Motor Matching	16
4.2	Design Approach	16
4.3	Performance Characteristics	18
4.4	Stability Analysis	21
4.5	Three-view drawings of the final design	21
5	Controls	22
5.1	Control Strategy	22
5.2	Flight Performance	22
6	Fabrication	22
6.1	Prototype Construction Approach	22
6.1.1	Mk-I "The Red Baron"	22
6.1.2	Mk-II "The Pig"	22
6.1.3	Mk-III.1	22
6.1.4	Mk-III.2 "Ronald McDonald"	22
6.1.5	Mk-III.2 "Terminator"	22
6.1.6	Mk-III.2 "The UltraLight"	22
7	Flight Testing	22
7.1	Flight Test Approach	22
7.2	Simulation vs. Actual Tests	22
8	Mission Flight Results	22
8.1	Official Flight Results	22
8.2	Analysis of Flight Data	24
9	Conclusions & Lessons Learned	24

1 Introduction

Since the early 2000's, Stanford Aeronautics and Astronautics has taught the AA 241X: Design, Construction and Testing of Autonomous Aircraft course with various missions over the years. In Spring of 2014, teams were tasked with developing an autonomous aircraft to search and accurately locate four targets within the perimeter of Lake Lagunita. Among these teams was Skynet, a group of eight individuals from different backgrounds and expertise who, throughout the ten weeks, collaborated to organize, design, test, and fly various aircraft, guidance, control, and mission systems to optimally complete the search and rescue. The following report outlines the team's structure, mission strategy, aerodynamic design, control strategy, fabrication accounts, flight test data, and overall competition performance.

2 The Team

2.1 Team Structure

2.2 Team Communication & Logistics

In order to facilitate group discussions, a when2meet form was utilized online. Based on its results, the team met briefly after class on Mondays and Wednesdays for brief sub team status updates and coordination. Major team meetings were held on Fridays during the typical class time on the second floor of Durand and were spent discussing topics requiring everyone's attendance such as aircraft design and mission strategy.

The team also utilized online methods to meet communication needs. A Google Group was utilized for formalized notices and e-mail discussions. Short-form and quick information relays were handled by a GroupMe that could be accessed via phone or computer.

Data Storage and problem set completion was made possible via our Google Drive, Google Docs, and a Wordpress. All team data, code, and photos were uploaded into categorically defined folders in our Google Drive. Spreadsheets recording budget, weather data, contact information, useful links, and most importantly, problem set requirements were also held here. Having all of these documents in a single location and accessible by all of the team was the last step in facilitating good communication and ensured proper problem set completion. Once written, relevant text, data, graphs, and videos were uploaded to skynet241x.wordpress.com.

3 Mission

3.1 Approach via identification of score components

Skynet's mission strategy, and subsequent airplane design, is motivated by the identification of bounds on the three components of score:

1. **Accuracy component:** Positive real, bounded above by $\alpha/4 = 50$ (perfect refinement) and below by 0 (estimates at infinity).

This suggests that we should have a high endurance aircraft and a specialized refinement algorithm.

2. **Time component:** Positive real, unbounded above (save for physical constraints) and bounded below by 0 (failure to locate one or more targets).

This suggests that we should have a trajectory that can locate all the targets with probability 1, and fly as fast as such a trajectory (and battery requirements) would admit.

3. **Reliability component:** Positive real, unbounded above (save for official flying period limits) and bounded below by 1 (less than 6 flights). Note, however, that $\delta_{rel} \sim 1 + 0.01n_{flights}$ as per the final scheme adopted for the competition, which implies that the overall average gets multiplied by only 1.5 after 50 flights.

This suggests that we should have control loops that can ensure identical inner loop performance on every run.

Based on the observations above, the finalized mission plan consists of two phases. Phase-1 consists of a passive search to locate all targets with complete certainty irrespective of the placement of the targets on the field. It includes an analytical trajectory that ensures that every point within the search domain lies within at least one of the snapshots. Phase-2 actively refines the sighted targets based on heuristic arguments of recursion. As an intermediate step, the order of visiting the sighted targets for refinement is decided through a brute force sorting of all possible paths. At the core of the mission plan is the numerical scheme for estimation of the target position based on the randomized values returned from the virtual camera.

3.2 Phase-1: An initial passive path to sight all targets with probability 1

The initial passive path attempts to solve the following variational problem:

Denote the target by ξ , Lake Lagunita by Ω , field of view by F , diameter of the FOV by f and snapshot by i . Let ξ be a uniformly distributed random variable in a closed simply connected subset Ω of \mathbb{R}^2 . Let $x^c \in \mathbb{R}^2$ be a smooth curve that has been discretized at n points $\{x_i\}_i^n$ so that each point of the discretized trajectory x_i is associated with a circular region $F_i = \{y \in \Omega : \|y - (x_{i_1}, x_{i_2})\| \leq f(x_{i_3})\}$. Find x_i that minimizes $L = \int_{x_i}^{x_n} \|dx^c\|$ such that $P(\xi \in \cup_1^n F_i) = 1$. The problem is constrained by the distance between snapshots which is bounded above due to maximum cruise speed and below due to the stall speed.

The initial approach to find a solution for this problem had been guided by parametric optimization of spiral-like trajectories. However, these optimal trajectories were quite sensitive to cruise airspeed of the aircraft and, more importantly, had a finite (although small) probability of failing to sight one of the four targets. The final strategy for phase 1 employs an analytical trajectory

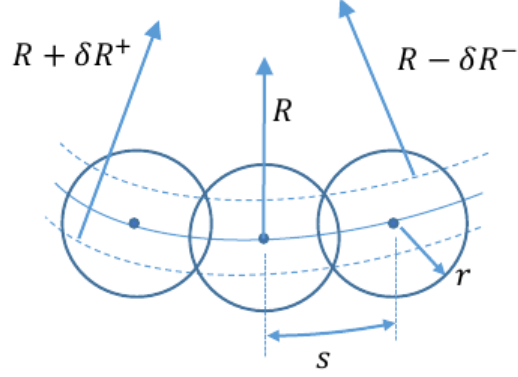


Figure 1: Annular region contained within discrete circles

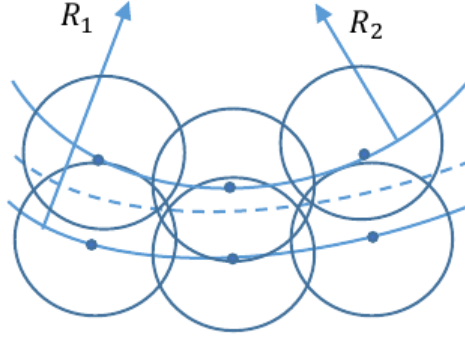


Figure 2: Overlap between subsequent annular regions

which by construction ensures that the search domain (Lake Lagunita) is a subset of the union of the fields of view across all snapshots. The existence of such a trajectory can be easily proven by observing that the union of intersecting circles of equal radii r , whose centers lie on the circumference of another circle of radius R , strictly contain an annular region of outer radius $R + \delta R^+$ and inner radius $R - \delta R^-$ (see figure 1), where δR^+ and δR^- are determined from the solution of the following non-linear equations:

$$d_k = R_k \left(2 \left(1 - \frac{\cos s}{R_k} \right) \right)^{1/2}$$

$$R_k + \delta R_k^+ - (R_k^2 - d_k^2/4)^{1/2} = (r^2 - d_k^2/4)^{1/2}$$

$$\delta R_k^- = 2 (r^2 - d_k^2/4)^{1/2} - \delta R_k^+$$

This suggests that the desired trajectory can be realized by a set of concentric circles whose radii R_i are chosen to ensure that corresponding consecutive annular regions have non-zero overlap (see figure 2).

The analytical values of R_i can now be obtained recursively as follows:

1. Recurrence relation: $R_k + \delta R_k^+ = R_{k-1} - \delta R_{k-1}^-$
2. Base case: $R_1 + \delta R_1^+ = R_0 = 165$

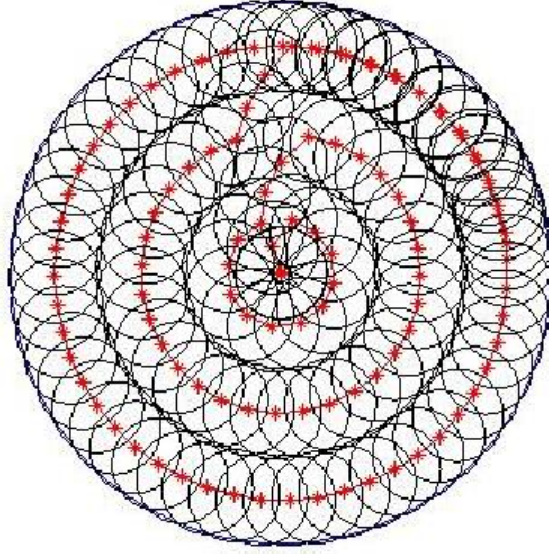


Figure 3: Typical trajectory used for phase-1

3. Parametric dependence: $s = v t_s$

where v is the cruise airspeed and t_s is the snapshot time gap.

Clearly, the trajectory is completely specified once the functional relationships of δR^+ and δR^- have been established. An instance of the passive trajectory for phase-1 is shown in figure 3.

3.3 Phase-2: An active path to refine the estimates of sighted targets

At the end of phase-1, each of the four targets ξ^j is known to lie within a simply connected and provably convex region ω^j with probability 1. Define a suitable norm on the region $\|\omega^j\|$. For our purpose, the geometric area or the maximum distance between any two points on the periphery of the region are appropriate measures. We are interested in finding a trajectory x_n^j for $n = 1, 2, 3, \dots, n_f$ such that the target region shrinks to a specified tolerance, i.e. the sequence ω_n^j converges so that $\|\omega_{n_f}^j\| < \|\omega_\gamma\|$ for a given tolerance $\|\omega_\gamma\|$. For an active trajectory, x_n^j depends on $x_1^j, x_2^j, \dots, x_{n-1}^j$. Given this requirement, we can identify certain key characteristics of the trajectory:

- The trajectory must lead to convergence for any admissible ξ^j and ω^j
- The discrete waypoints on the trajectory must be navigate-able within performance constraints
- The determination of the trajectory must not be computationally intensive

For this phase of the mission, we augment the estimation procedure (see section 3.4) by keeping track of unsuccessful snapshots (those that did not contain the target) as well. The target region is then obtained by first evaluating the intersection of all successful snapshots and then exsecting the union of unsuccessful snapshots. The subsequent procedure is the same as before. Note that the estimation strategy guarantees that $\|\omega_n^j\|$ is a non-increasing sequence.

One possible active trajectory that satisfies the essential requirement of convergence can be obtained through heuristic arguments. Let v be the cruise airspeed dictated by design for maximum endurance, R_f be the radius of the field of view at the highest admissible altitude, t_s be the snapshot gap time, and radius R be an intrinsic parameter. Then:

1. Evaluate y_n the centroid of ω_n
2. Let $x_{n1} = y_{n1} + R \cos(v t_s/R)$, $x_{n2} = y_{n2} + R \sin(v t_s/R)$ i.e. follow a circular path of radius R centered at the centroid of the target region
3. Evaluate the field of view and check for presence of target.
 - a If a target is found, evaluate ω_{n+1} using all the snapshots. Then repeat steps 1-3
 - b Otherwise, set $\omega_{n+1} = \omega_n$ and repeat steps 2-3

The exit criterion used for determining convergence has been taken to be $\|\omega_{n_f}\| < 1$ which approximately corresponds to the norm of the region being smaller than $\gamma = 1m$. The parameter R is taken to be equal to $R_f \sim 30m$, and v is taken to be $5m/s$.

In words, this active path is composed of ‘shifting circles’ where the changing circles correspond to levels of the algorithm. Several very interesting geometrical convergence statements can be proven. However, instead of delving deep into theoretical results, we briefly comment on the salient features of the process that are directly related to the key characteristics outlined above.

- The algorithm is guaranteed to converge for any admissible target location and target region provided that $v < (2\pi R)/3$. In fact, the convergence is proportional to $\sqrt{n_l}$ where n_l is the level of the algorithm. This follows from the fact that during each level of the algorithm the area of the region decreases on average by at least a factor of $1/3$ due to the following geometric result: A circle of radius R can be equi-partitioned by 3 circles of radii R centered at the vertices of an equilateral triangle inscribed within the original circle.
- The radii of the circles for any level of the algorithm is fixed to be $R = R_f \simeq 30m$. Since v is taken to be $5m/s$, the required rate of turn is very low and the waypoints can be navigated easily.
- The simplicity and strength of this method lies in the recursion among levels. The definition of the trajectory is dependent on the target region only through the centroid. Thus, no special treatment is required as the target region shrinks. The altitude is kept fixed at the highest admissible value. Clearly, the generation of waypoints is computationally simple.
- The performance of the algorithm is fairly robust with respect to small variations in the possible parameter set - R, v , altitude etc.

An instance of the refinement procedure for a randomly generated target starting from a single snapshot (worst case scenario at the end of phase-1) is shown in figure 4. The ‘x’ mark is the true target, the ‘+’ marks are estimates returned by the camera, the diamonds are processed target locations, and ‘*’ denote the target region. A portrait of the successful and unsuccessful snapshots is shown in figure 5. Figure 6 plots the convergence history of the algorithm through a geometrical as well as an exact measure.

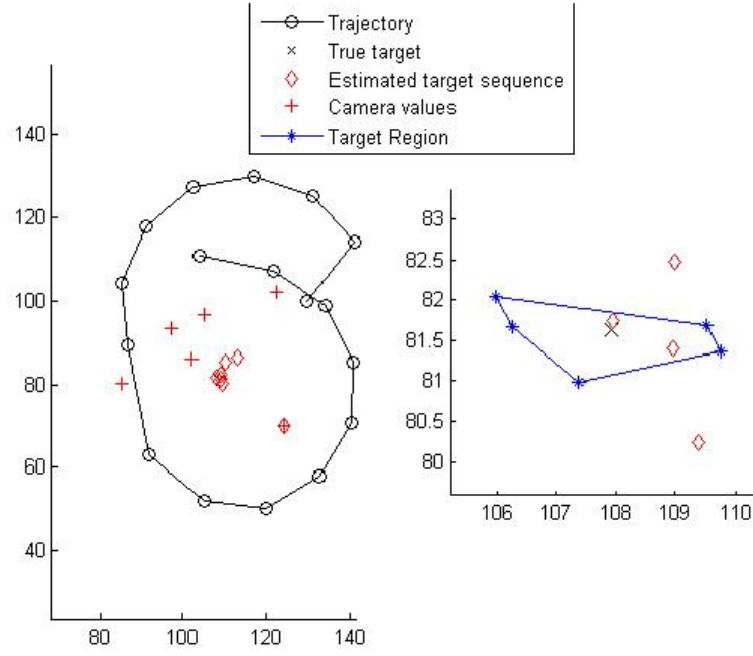


Figure 4: An instance of the refinement procedure

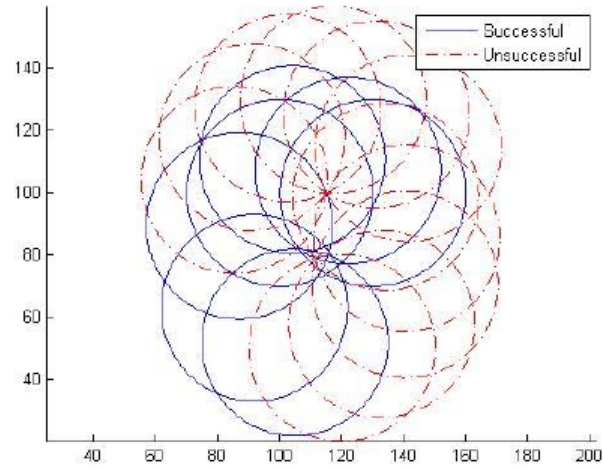


Figure 5: A portrait of the successful and unsuccessful snapshots

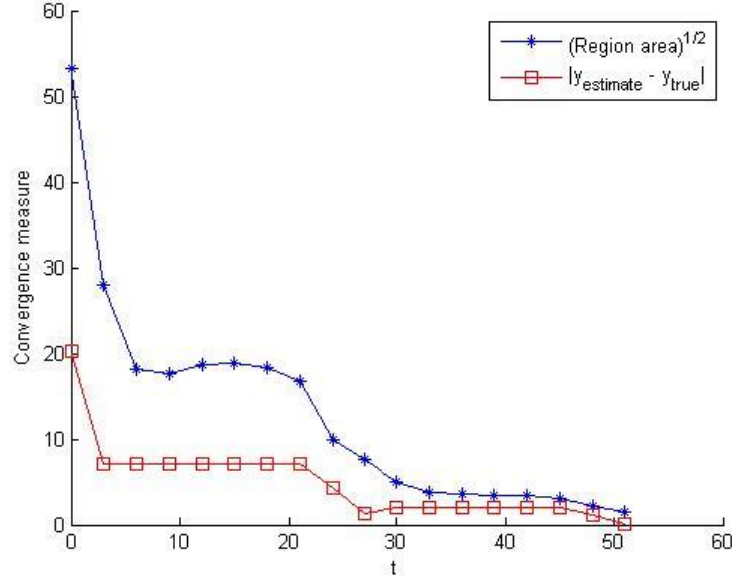


Figure 6: Convergence history of the algorithm

3.4 Target position estimation scheme

Skynet's target position estimation algorithm is based upon the following two observations:

1. The camera reports an estimate only when the true target is located within the FOV. Hence, after K_j successful snapshots for the j^{th} target, the target must be located in $\cap_i^{K_j} F_{j_k}$ with probability 1.
2. The estimates $y_{est_{j_k}}$ returned from the camera for the j^{th} target are drawn from a bivariate normal distribution with mean $(y_{true_{j_1}}, y_{true_{j_2}})$ and finite expectation. The maximum likelihood estimator for this case is exactly the sample mean

$$(\hat{y}_{j_1}, \hat{y}_{j_2}) = \frac{1}{K_j} \left(\sum_1^{K_j} y_{est_{j_{k_1}}}, \sum_1^{K_j} y_{est_{j_{k_2}}} \right)$$

The following asymptotic results provide theoretical reliability to the two measures mentioned above

1. Let $F_i = \{y : \|(y_1, y_2) - (y_{i_1}, y_{i_2})\| \leq r, \|(\xi_1, \xi_2) - (y_{i_1}, y_{i_2})\| \leq r\}$ denote circular areas with radius r centered at y_i that all necessarily contain the point ξ . Further let y_i be drawn from a uniform random distribution in \mathbb{R}^2 . Then, $P(\|y_n - \xi\| > \delta) \rightarrow 0 \quad \forall \quad y_n \in \cap_i^n F_i, \delta > 0$ as $n \rightarrow \infty$.

In other words, the intersection of the random circles converges to the common point. Hence, if we take enough snapshots, the fields of view alone would be enough to provide us with the true location of the targets.

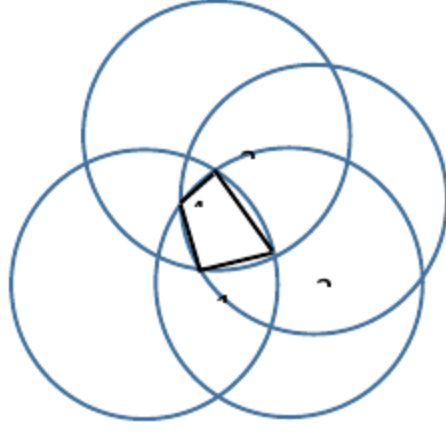


Figure 7: Region that contains the target with probability 1

2. The maximum likelihood estimator is asymptotically convergent (i.e. consistent)

Hence, if take enough snapshots, the random estimates from camera alone would provide us with the true location of the targets.

The actual implementation of the above procedure is relatively complicated. While the sample mean of estimates is easy to calculate, the intersection of circles is more involved. Similarly, the process of ensuring that the final estimate falls within this intersection is another task. Skipping over the details for brevity, we provide here a flowchart of the process for each target:

1. 1. Find a discrete representation of the region of intersection of the FOV circles - I

Scheme: The intersection of n circles (that all contain a common point) results in $\binom{n}{2}$ intersection points. Out of these, only $p \leq n$ points lie on the periphery of the intersection of the circles. The necessary and sufficient condition for these points z_m for $m = 1, 2, \dots, p$ is given by

$$\|z_m - y_i\| \leq R_i \text{ for } i = 1, 2, \dots, n$$

where y_i are circle centers, and R_i the radii.

Owing to the convexity of circular arcs, these p points result in a p -sided convex polygon (see figure 7).

2. Find the sample mean of the estimates returned by the camera \hat{y}
3. Check if $\hat{y} \in I$. If yes, report \hat{y} as the final estimate (see figure 8).

Scheme: Standard geometric algorithm for detecting if a point lies inside a convex polygon.

4. If $\hat{y} \notin I$ report y_{target} as the point in I that is 'close' to \hat{y} .

Scheme: Find the point of intersection of the line joining centroid of the polygon and \hat{y} with the perimeter of the polygon. (see figure 9)

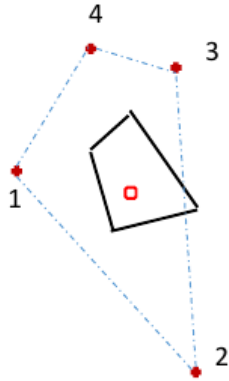


Figure 8: MLE within geometric requirements

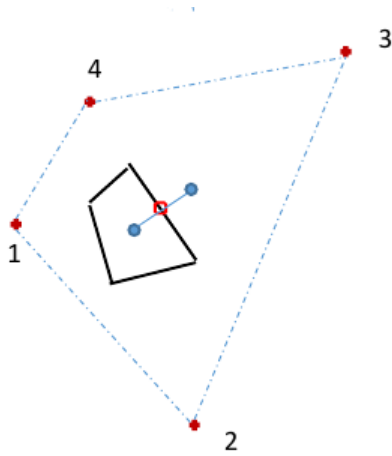


Figure 9: Geometric correction to MLE

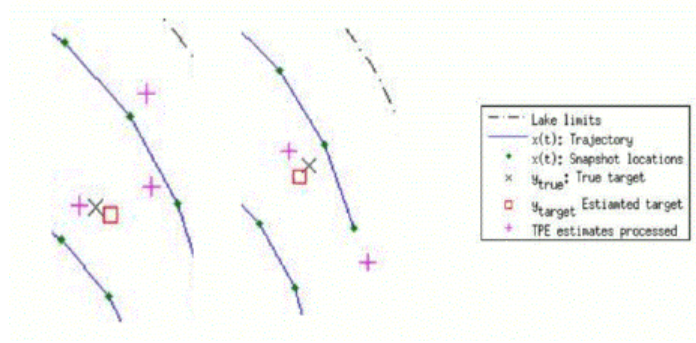


Figure 10: Performance of estimation algorithm

Figure 10 shows the advantage of this estimation method during actual simulations. The ‘x’marks are the true targets, the ‘+’marks are estimates returned by the camera, and the squares are processed target locations.

3.5 Statistical measure of score and mission time

As per the analysis of the aircraft performance group, the finalized aircraft design was expected to have maximum endurance near stall speed. For this purpose, the airspeed for Phase-2 was simulated at $5m/s$. (Actual flight tests later revealed that the airplane stalled around $7m/s$ and, incidentally, could operate stably only above $9m/s$).

Similarly, the optimal rate of climb at the beginning of Phase-1 was simulated as per design values. The only free parameter remaining was the cruise speed during phase-1. Towards this aim, a parametric study with cruise airspeed was conducted by gathering statistics over 100 realizations of the target locations.

Figure 11 plots the variation of the sample mean of the two components of score (β/t_{sight} and $\alpha/\sum_{i=1}^4 \max(\gamma, \|y_{target} - y_{true}\|)$) and the total score along with their standard deviations as error bars. We note that

- The accuracy component is very close to its maximum value (~ 50) for $v \leq 11m/s$
- The t_{sight} component increases with v for $v \leq 12m/s$ after which the battery gets consumed for some realizations even before phase-1 can be completed
- The accuracy component for $v = 12m/s$ is reduced due to excessive battery consumption during phase-1
- From a-c, we conclude that $v = 11m/s$ is the ideal cruise speed for phase-1

It is important to mention that these observations should have been ideally dictated by actual flight tests rather than empirical estimates. However, the final implementation, integration and debugging of the airplane system did not leave much time for testing and fine tuning.

Figure 12 plots various components of mission time for such cases where all targets could be located before the battery was consumed. As expected, t_{sight} does decrease with v under this restriction. The refinement times start to go down for $v \geq 12m/s$ as the targets are not fully refined before the battery is consumed, and are therefore not plotted on the graph below.

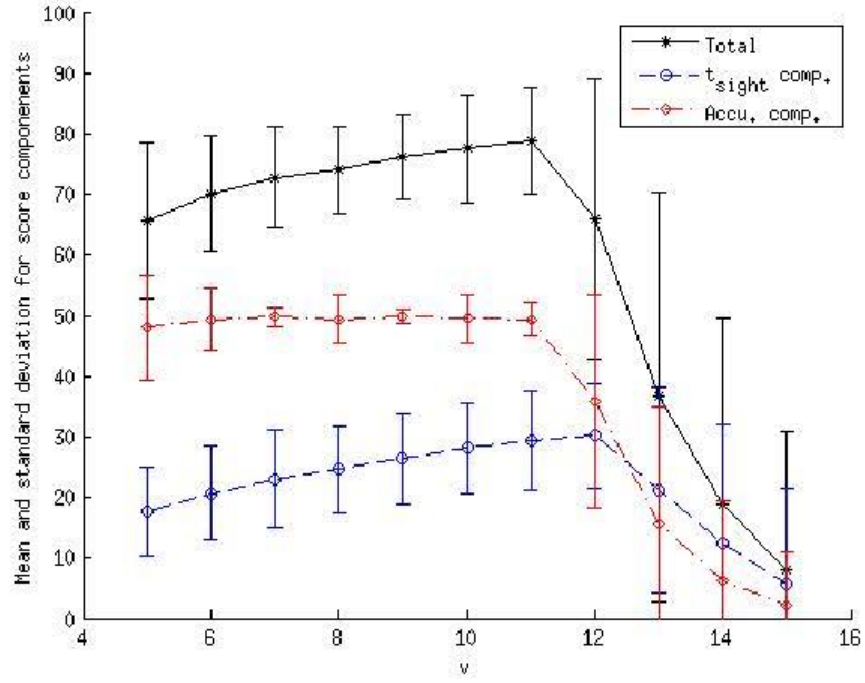


Figure 11: Mean and standard deviation for score components

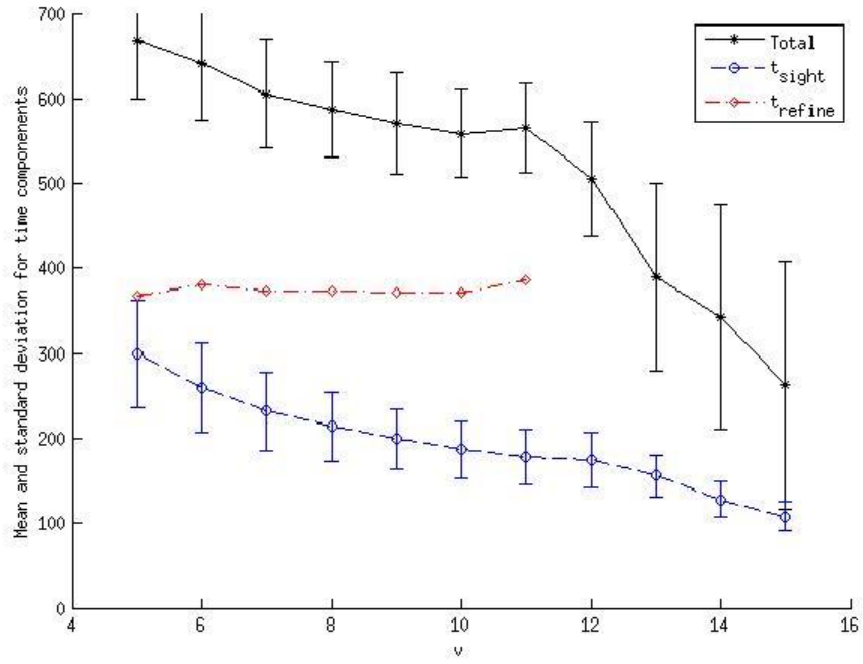


Figure 12: Mean and standard deviation for time components

Finally, the statistics for the chosen parameter values are tabulated below. This is the theoretical expectation of the mission values.

Quantity	Component	Mean	Standard dev.
Score	Total	78.3	9.3
	Accuracy	49.3	4.1
	t_{sight}	29.0	8.2
Time	Total	557.0 s	56.1 s
	t_{sight}	180.9 s	33.0 s

4 Airframe Design

4.1 Propulsion System Analysis

The propulsion system analysis was performed in three parts:

1. Propeller analysis
2. Motor analysis
3. Propeller and Motor matching

4.1.1 Propeller Analysis

For the propeller analysis, we used wind tunnel experimental data from the UIUC Propeller Data Site ¹. The exact same propeller data was unavailable in the database, so we used a very similar propeller (Graupner CAM Slim 9x5) albeit from a different manufacturer.

The data was given in terms of the rotations per second instead of the angular velocity and hence, the following scaling had to be performed

$$\begin{aligned}\lambda &= \frac{J}{\pi} \\ C_T &= \left(\frac{2}{3}\right)^3 C'_T \\ C_P &= \frac{1}{\pi} \left(\frac{2}{3}\right)^3 C'_P \\ \eta &= \eta'\end{aligned}$$

where λ is the advance ratio based on the angular velocity, J is the advance ratio based on the rotations per second, C_T is the thrust coefficient, C_P is the power coefficient and η is the propeller efficiency. The primed quantities are the ones reported in the database.

4.1.2 Motor Analysis

The motor analysis was performed by using the standard electric motor model. The motor speed constant, motor resistance and the no-load motor current were obtained from experimentally measured values on the manufacturer's website ².

The values of the model constants are reported below:

$$\begin{aligned}K_v &= 980 \left(\frac{2\pi}{60}\right) \text{ rad/s/volt} \\ R_m &= 0.220 \, \Omega \\ i_0 &= 0.4 \, A\end{aligned}$$

¹<http://aerospace.illinois.edu/m-selig/props/propDB.html>

²<http://www.maxxprod.com/pdf/HC2808-xxxx.pdf>

4.1.3 Propeller and Motor Matching

For a given free-stream velocity, the required torque for the propeller was calculated as a function of the angular velocity of the propeller. For the motor, the torque generated was calculated as a function of the angular velocity. By matching these two torques, we solved for the angular velocity and obtained the total propulsive efficiency. This process is illustrated in Figure 13.

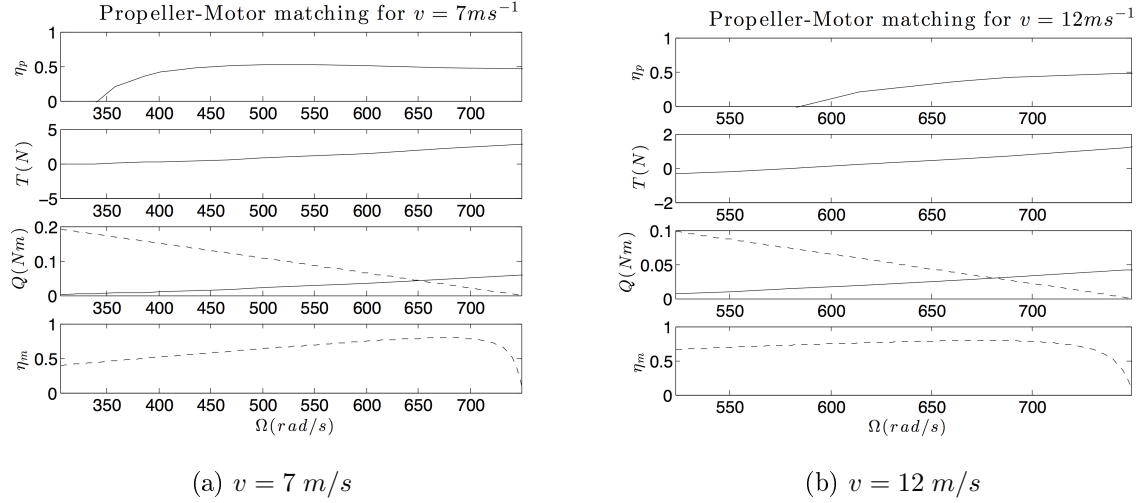


Figure 13: Propeller-Motor matching shown graphically. Solid lines: propeller curves. Dashed lines: Motor curves

For the 7 ms^{-1} case, we see that the propeller efficiency, η_p peaks at very low angular velocities and hence the total propulsive efficiency is poor. For the 12 ms^{-1} case, the propeller efficiency, η_p peaks at high angular velocities which again leads to a low total propulsive efficiency. Optimizing the total propulsive efficiency over different airspeeds, we get the best motor-propeller matching illustrated in Figure 14

The total propulsive efficiency and the thrust are plotted against airspeed in Figure 15.

4.2 Design Approach

For our mission plan, it is critical that we climb to an altitude of 400 ft as fast as we can to efficiently scout the search area and sight all four targets as soon as we can. Hence, the rate of climb for our airplane is of crucial importance. In addition to this, the endurance of our aircraft is also very important since the allowed battery consumption is very limiting. We designed our aircraft mainly based on these two considerations.

First, we obtained the drag polar for a generic 2D semi-symmetrical airfoil section (Clark-Y) in XFLR5 that we used as our first estimates for our full aircraft drag polar. From some preliminary weight estimates, we allotted a 450 g weight budget for our aircraft. Using this weight and the 2D drag polars data, we found the wing area that would maximize our rate of climb using the data from the analysis of the propulsion system. We chose a taper ratio of 0.5 for our wing. This choice was influenced by structural constraints on the total root bending moment and the stall characteristics so that in the event of a stalled aircraft, aileron control is not lost. Then, we assumed an aspect

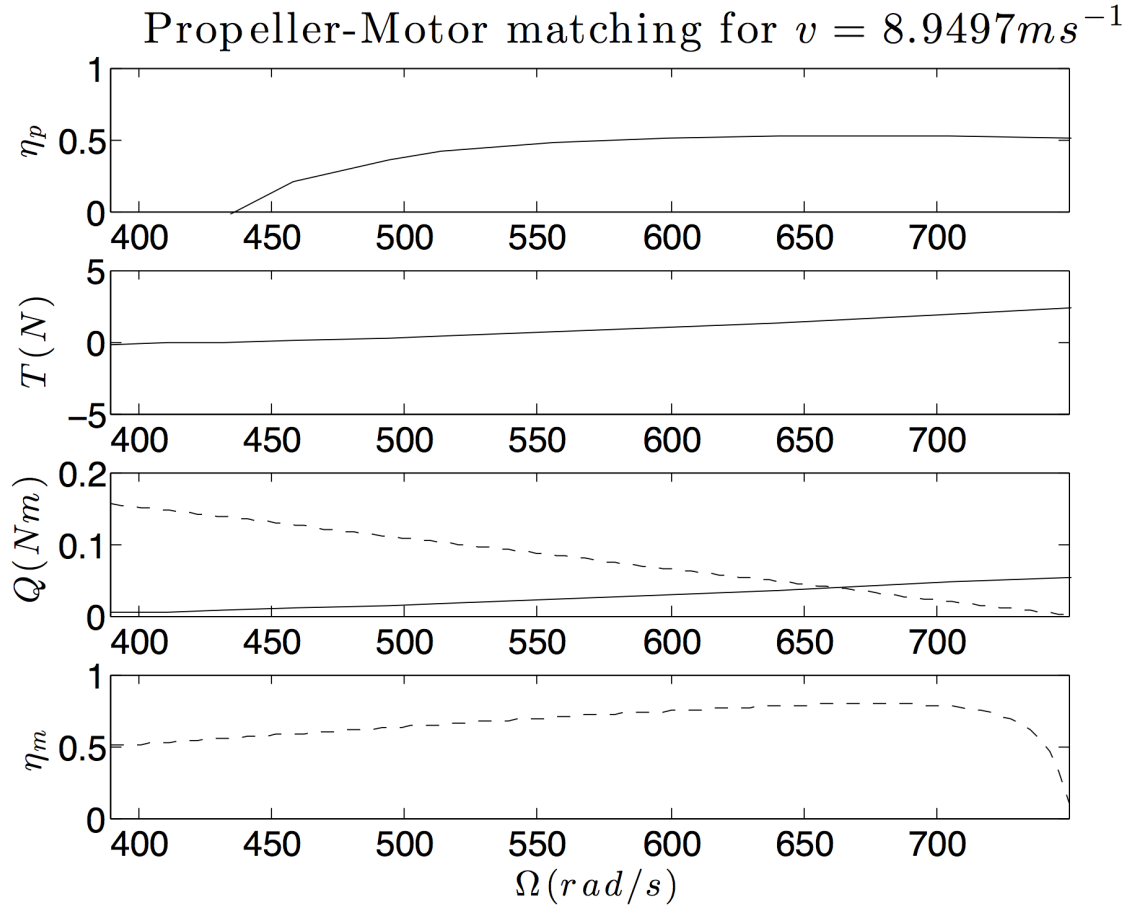
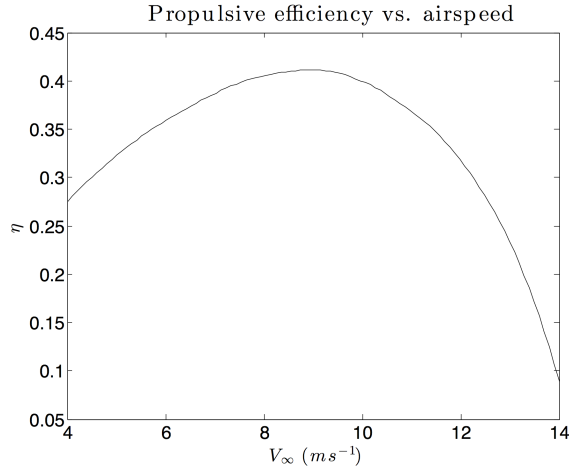


Figure 14: Optimal Propeller-Motor matching shown graphically. Solid lines: propeller curves. Dashed lines: Motor curves

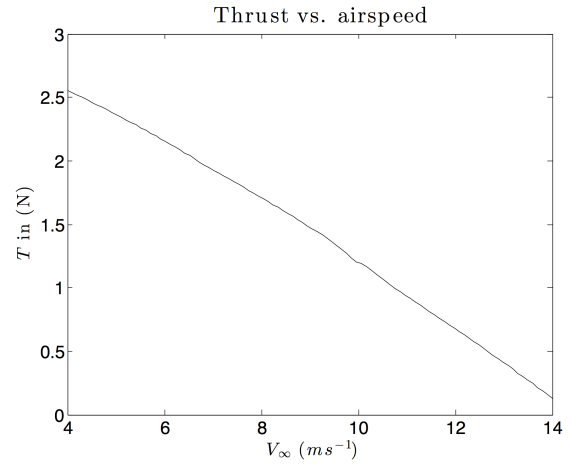
ratio of 6.8 (that of the Bixler 2). This allowed us to construct a wing in XFLR5 to get a more realistic drag polar. This process was repeated iteratively until convergence. However, we changed our aspect ratio to 10 since we felt it would be possible to make a wing with that aspect ratio that is still rigid enough.

After this preliminary analysis, we did the same analysis with different airfoil sections and chose the SD-7037 airfoil section since the predicted $(L/D)_{max}$ was the highest for this airfoil. The effect of the choice of airfoil section on the climb performance was found to be minimal and hence we were able to perform a decoupled analysis for the choice of airfoil sections.

Then, we calculated the horizontal stabilizer area from considerations of the longitudinal stability that were backed by Vortex Lattice Model predictions. The vertical stabilizer size was chosen based on previous aircraft designs similar to our aircraft and then validated using stability analysis in AVL.



(a) Plot of the total propulsive efficiency against airspeed



(b) Plot of the total thrust against airspeed

Figure 15: Thrust and efficiency plots

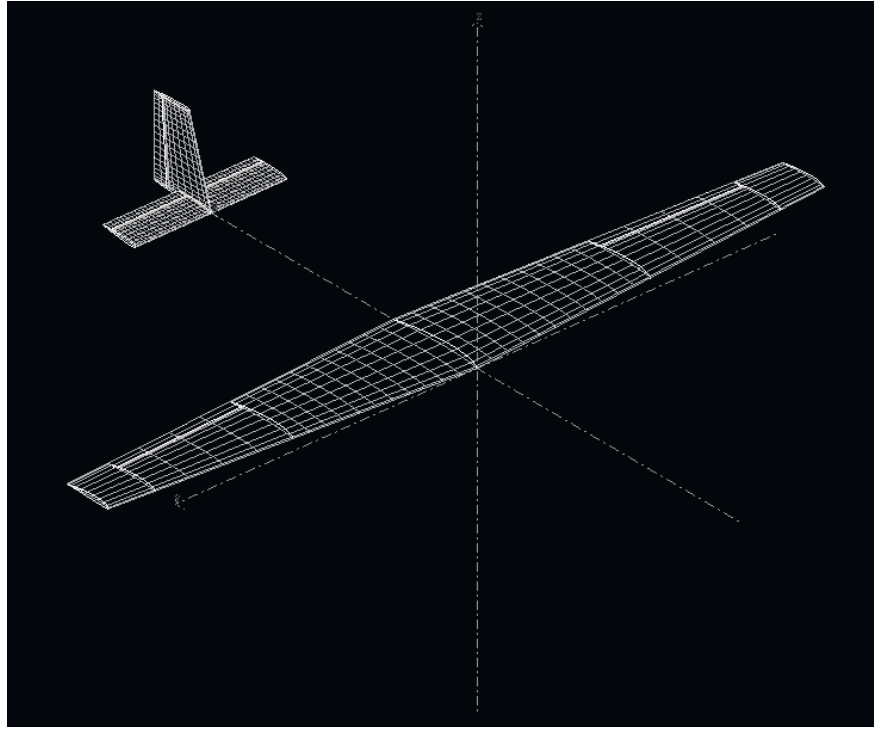


Figure 16: VLM model of our design in XFLR5

4.3 Performance Characteristics

The different performance parameters of our design as predicted by XFLR5 are shown in Figures 17 to 21.

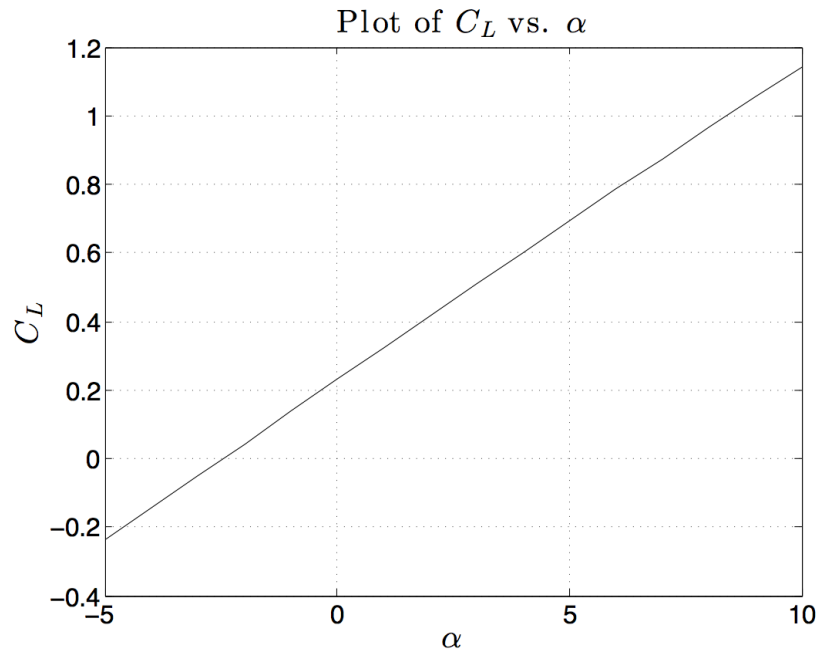


Figure 17: C_L vs α

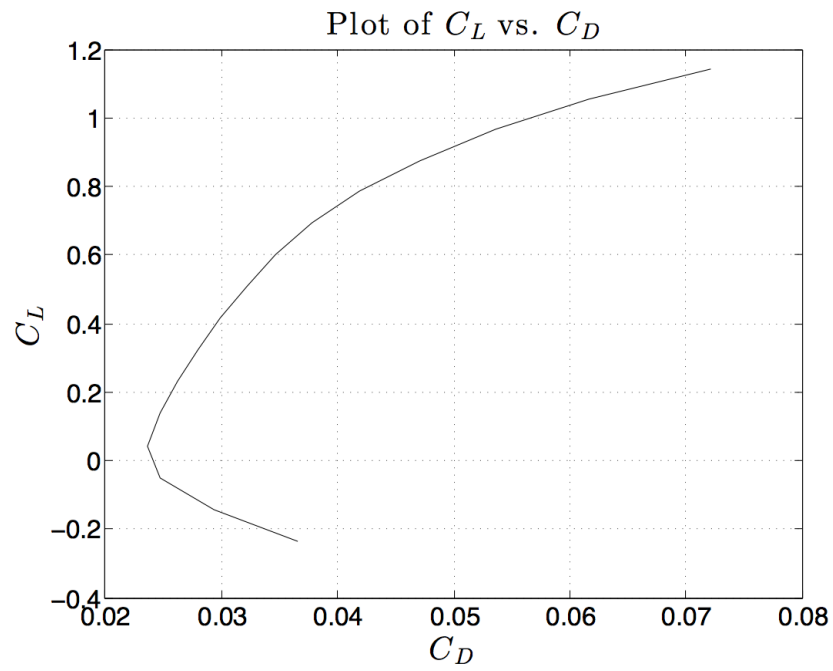


Figure 18: Drag polar

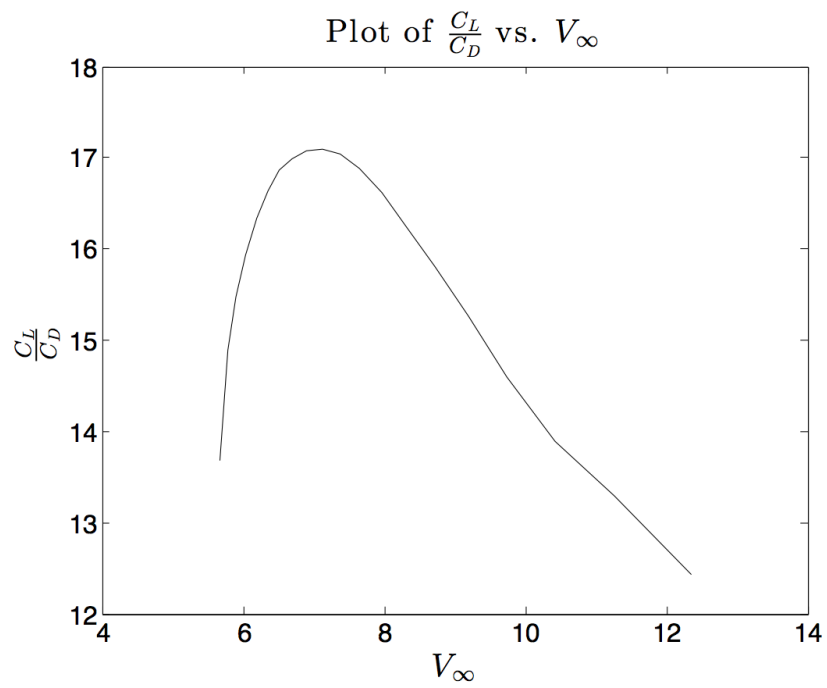


Figure 19: C_L/C_D vs v_∞

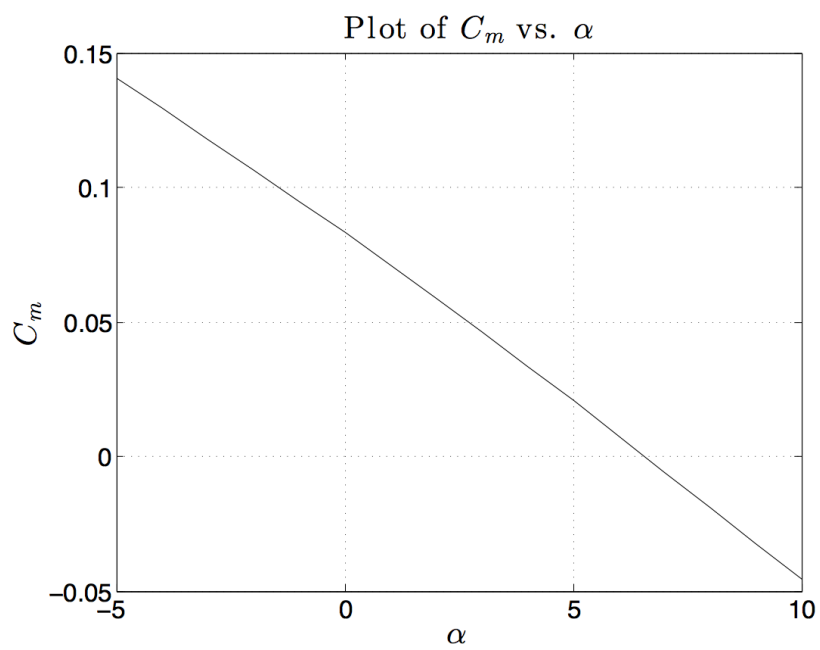


Figure 20: C_m vs α

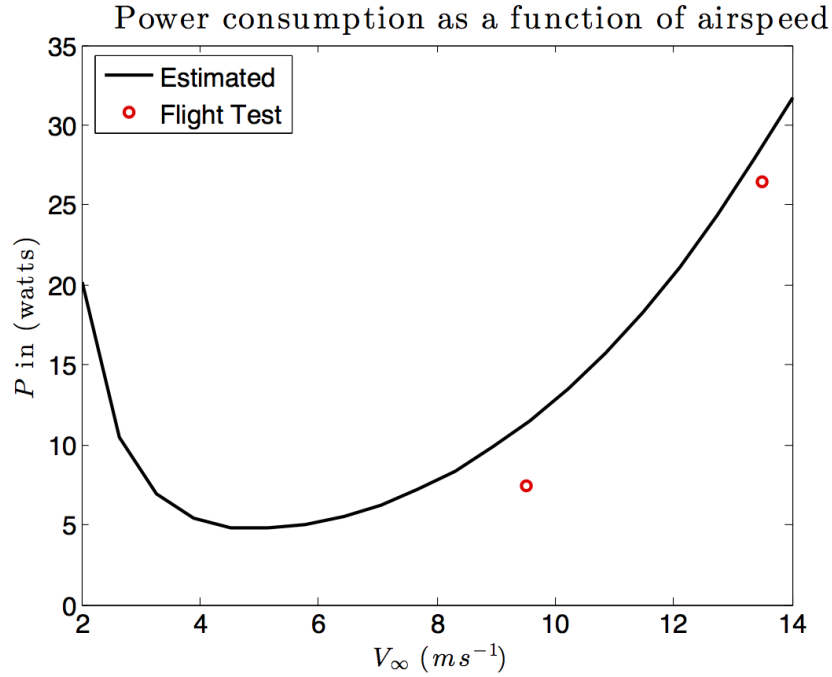


Figure 21: P_{level} vs airspeed

A comparison of the performance parameters estimated from our analysis with the performance parameters obtained from measured data during flight tests is shown in Table 1.

	$C_L max$	$(L/D)_{max}$	$P_{level} (9.5 ms^{-1})$	$P_{level} (13.5 ms^{-1})$	$P_{max climb}$
Estimated	1.14	19.0	11.29 watts	28.62 watts	34.12 watts
Measured	0.73	16.3	7.45 watts	26.47 watts	39.98 watts

Table 1: Estimated vs. measured flight performance parameters

4.4 Stability Analysis

The stability analysis of our design was performed in AVL. Three different straight and level flight trim states and one level turn trim state were analysed. The four cases used are listed in Table 2.

The eigenvalues, frequencies and damping ratios for the different modes are plotted in Figures 22, 23 and 24.

4.5 Three-view drawings of the final design

Figure 25 shows the CAD drawings of our final design. Figure 26 shows the SolidWorks model of our design that we used to get all the parts for the laser cutter.

Case	Airspeed (in m/s)	Bank Angle (in degrees)
Case 1	8.5	0
Case 2	7.0	0
Case 3	10.0	0
Case 4	8.5	30

Table 2: Different cases for stability analysis in AVL

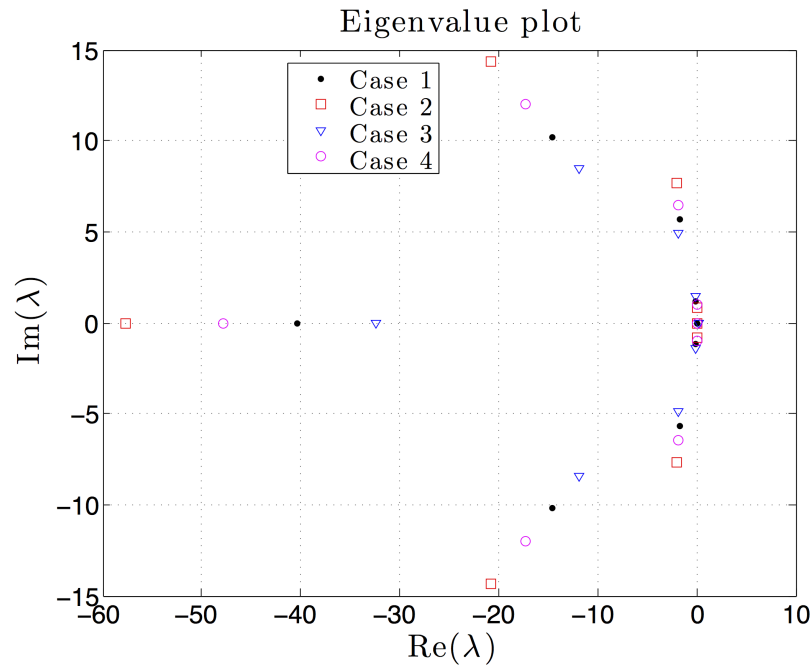


Figure 22: Eigenvalue plot

5 Controls

5.1 Control Strategy

5.2 Flight Performance

6 Fabrication

6.1 Prototype Construction Approach

6.1.1 Mk-I "The Red Baron"

6.1.2 Mk-II "The Pig"

6.1.3 Mk-III.1

6.1.4 Mk-III.2 "Ronald McDonald"

6.1.5 Mk-III.2 "Terminator"

6.1.6 Mk-III.2 "The UltraLight" 22

7 Flight Testing

7.1 Flight Test Approach

7.2 Simulation vs. Actual Tests

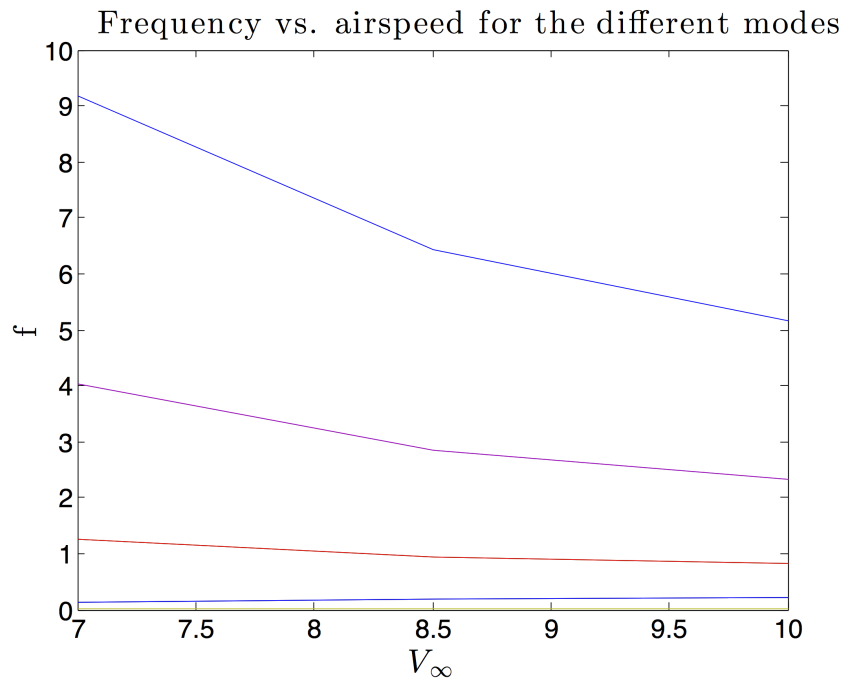


Figure 23: Frequency

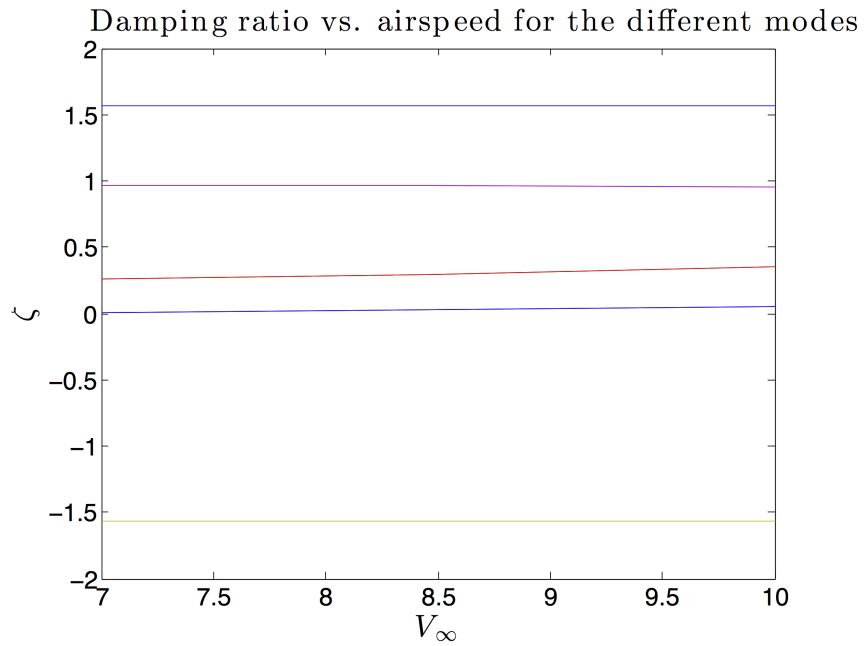
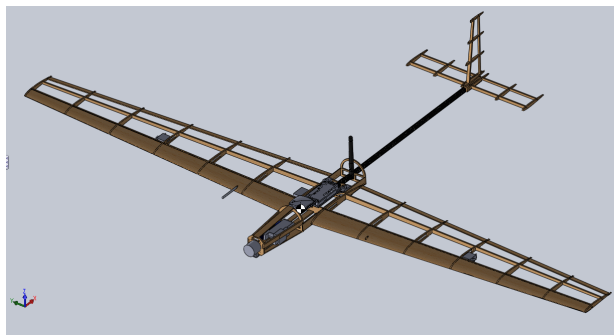


Figure 24: Damping ratio

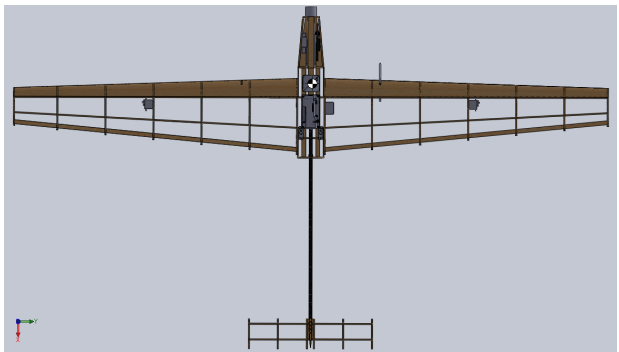
8.2 Analysis of Flight Data

9 Conclusions & Lessons Learned

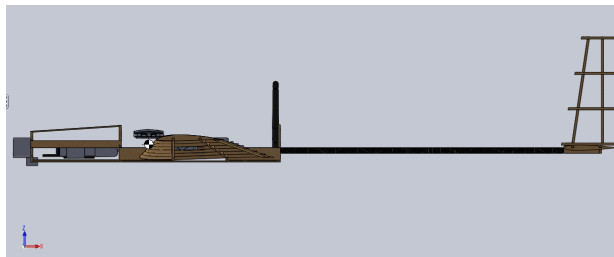
10 Future AA241X Recommendations



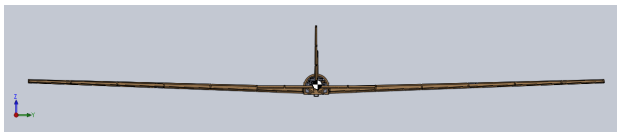
(a) Isometric view



(b) Top view



(c) Side view



(d) Front view

Figure 26: Solidworks model screenshots